Satellite microwave remote sensing of North Eurasian inundation dynamics: development of coarse-resolution products and comparison with high-resolution synthetic aperture radar data

R Schroeder[1], M A Rawlins[1], K C McDonald[1], E Podest[1], R Zimmermann[2] and M Kueppers[2]

[1] Jet Propulsion Laboratory, California Institute of Technology, 4800 Oak Grove Drive, Pasadena, CA 91109, USA
[2] University of Hohenheim, D-70593 Stuttgart, Germany

E-mail: ronny.schroeder@jpl.nasa.gov

Abstract
Wetlands are not only primary producers of atmospheric greenhouse gases but also possess unique features that are favourable for application of satellite microwave remote sensing to monitoring their status and trend. In this study we apply combined passive and active microwave remote sensing data sets from the NASA sensors AMSR-E and QuikSCAT to map surface water dynamics over Northern Eurasia. We demonstrate our method on the evolution of large wetland complexes for two consecutive years from January 2006 to December 2007. We apply river discharge measurements from the Ob River along with land surface runoff simulations derived from the Pan-Arctic Water Balance Model during and after snowmelt in 2006 and 2007 to interpret the abundance of widespread flooding along the River Ob in early summer of 2007 observed in the remote sensing products. The coarse-resolution, 25 km, surface water product is compared to a high-resolution, 30 m, inundation map derived from ALOS PALSAR (Advanced Land Observation Satellite phased array L-band synthetic aperture radar) imagery acquired for 11 July 2006, and extending along a transect in the central Western Siberian Plain. We found that the surface water fraction derived from the combined AMSR-E/QuikSCAT data sets closely tracks the inundation mapped using higher-resolution ALOS PALSAR data.

Keywords: inundation, dynamics, wetland, extent, Eurasia, microwave, AMSR-E, QuikSCAT, ALOS PALSAR

1. Introduction

Research on arctic climate change has suggested an unprecedented increase in heat transport toward the north because of a systematic change in atmospheric circulation (Zhang *et al* 2008). Concurrent with this alteration may be the recently observed dramatic loss of sea-ice (Serreze *et al* 2003, Comiso *et al* 2008), increasing terrestrial net primary productivity (Zhang *et al* 2007), accelerated arctic river discharge (Peterson *et al* 2002) as well as above-average arctic surface temperatures (Frey and Smith 2003) which ultimately drive arctic hydrological and biological processes (Serreze *et al*

2000, Kimball *et al* 2006). Associated with these reported arctic environmental changes may be increased greenhouse-gas emissions from lakes (Zimov *et al* 1997, Walter *et al* 2006) and thawing permafrost (Romanovsky *et al* 2002, Zimov *et al* 2006). Currently it remains speculative to which degree lake and wetland dynamics are affected by climate change, particularly for Siberia where vast geographical extent and weather conditions render year-round *in situ* observation of surface water patterns difficult. Satellite remote sensing is thus particularly advantageous for complete synoptic study of the behaviour of surface water dynamics across Northern Eurasia, allowing useful inference of recent greenhouse-gas emissions as well as supporting prediction of future processes.

Using optical satellite remote sensing, Smith *et al* (2005) have shown a net reduction in Siberian lake abundance and area. In contrast, Grippa *et al* (2007) and Mialon *et al* (2005) both using passive microwave radiometry confirm a positive surface water trend along the Ob River which the authors explain with a positive trend in river discharge and precipitation. A study carried out by Pavelsky and Smith (2008) over wetlands in Canada suggests that a significant change in river water level may point to differences in surface water patterns that cannot be explained by theoretical models of floodplain recharge.

This letter presents a remote sensing technique for determining surface water fraction based on combined passive–active microwave remote sensing data sets. This work focuses on Northern Eurasia, and a comparison of observations over two years, 2006 and 2007. Combined discharge from the six largest river basins in Eurasia reached a historical high in 2007, approximately 25% above the long-term mean (Shiklomanov and Lammers 2009, Richter-Menge *et al* 2008). We employ passive microwave data from advanced microwave scanning radiometer-EOS (AMSR-E) on NASAs Earth observing system (EOS) aqua satellite and active radar backscatter from the SeaWinds scatterometer on the QuikSCAT satellite platform (QSCAT) to derive surface water fraction at 10 day intervals across Northern Eurasia. We compare average basin surface water values from our coarse-resolution satellite product directly to river discharge measured at the mouth of the Ob River at Salekhard. We employ maps of total simulated runoff as determined with the Pan-Arctic Water Balance Model (PWBM) of Rawlins *et al* (2003) across the study domain to examine the variability in surface water for the two years studied as related to the springtime snowmelt. We compare our surface water product directly to a high resolution, independently developed land cover product derived from the phased array L-band synthetic aperture radar (PALSAR) data on the Japan Aerospace Exploration Agency's Advanced Land Observation Satellite (ALOS).

2. Study area

Our study area extends from 0 to 180° East longitude and 55°–90° North latitude. This region includes six large Arctic-draining river basins, the Ob, Yenisei, Pechora (P), Severnaya Dvina (SD), Lena and Kolyma (figure 1). The Ob and Yenisei River basins contain the world's largest known wetland
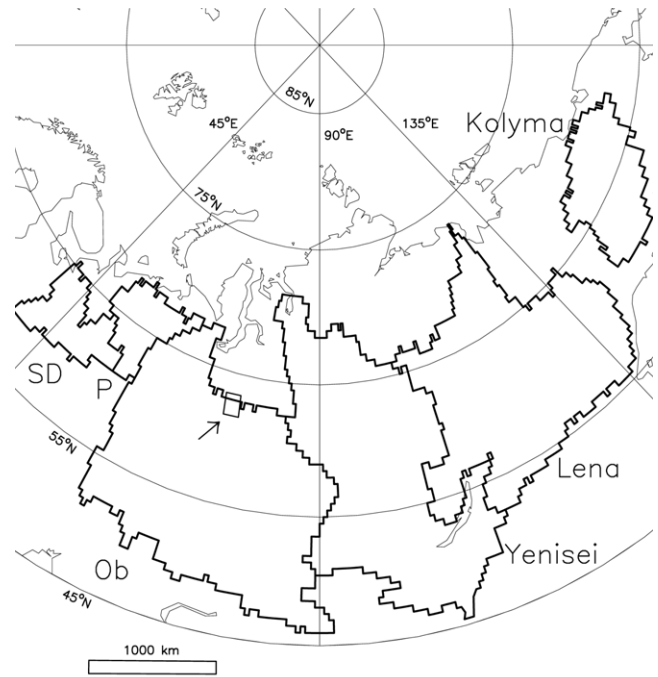

Figure 1. Location of the study area with the major river basin areas delineated (darker lines). Basin names are plotted for each basin (SD = Severnaya Dvina and P = Pechora). The ALOS PALSAR transect is located in the northern Ob river basin (arrow).

complex within the central Western Siberian Plain. This area is covered by boreal forest in the south, taiga in the middle and Arctic tundra in the north. Because of the continental location of these basins, permafrost is common with the growing season lasting only a few months (Kimball *et al* 2004).

3. Data and methodology

Posted to the 25 km × 25 km EASE-Grid, passive and active microwave satellite data from AMSR-E and QSCAT provide daily coverage of the study region. Microwave emissivity has been shown to be sensitive to large-scale surface water patterns because the emissivity of open water surfaces is very small relative to other land surface types (Giddings and Choudhury 1989, Choudhury 1991, Sippel *et al* 1994, Prigent *et al* 2001, Fily *et al* 2003, Mialon *et al* 2005, Temimi *et al* 2005, Grippa *et al* 2007). Passive microwave polarization difference ratios are derived from Level 2A dual-polarized AMSR-E radiometer brightness temperature (T_b) data (Knowles *et al* 2006) at 6.9 GHz to support derivation of the surface water fraction. We employ the microwave polarization difference index (MPDI) defined as:

$$\text{MPDI} = (T_{b(V)} - T_{b(H)})/(0.5(T_{b(V)} + T_{b(H)})) \qquad (1)$$

where $T_{b(v)}$ and $T_{b(h)}$ are the brightness temperatures at vertical and horizontal polarization, respectively. Use of the MPDI helps to account for the effects of surface temperature variations on brightness temperature (T_b), hence leaving a quantity that is largely dependent on the emissivity contributions from water surfaces, vegetation and soil moisture

within the satellite footprint (Njoku *et al* 2003). We employ only AM (morning) AMSR-E overpasses in this analysis in order to capture surface conditions as close to isothermal as practical to optimize this approach. Comparing boreal with tundra sites across Alaska and Northern Canada, Jones *et al* (2007) demonstrated that open water increases the AMSR-E polarization ratio most efficiently at lower frequencies, whereas over grassland a decrease in the polarization ratio may be attributed to the depolarization effect of a developing leaf canopy.

To account for the depolarization effect vegetation has on total pixel emissivity, a mixture model of active and passive microwave observations is used to quantify sub-pixel surface water fractions (figure 2). We use Level 2A HH-polarized QSCAT backscatter observations to maximize sensor sensitivity to the presence of vegetation biomass in inundated areas, maximizing backscatter dependence on scattering within the vegetation medium. Figure 2 shows this relationship for all snow free land pixels between January 2006 and December 2007 within the study domain. For each vegetation density range delineated by QSCAT backscatter σ_o, we determined two end-members (minimum and maximum) between which sub-pixel surface water fraction varies linearly. A direct comparison with several lake-dominated pixels fully covered by water (MPDI of ~0.67) reveals that total surface water fraction may be varying between ~10 and ~60%, assuming that, for the driest pixels in figure 2, the depolarization effect from the vegetation varies linearly between zero (at −20 dB with MPDI of ~0.067) and 10% (at −10 dB with MPDI of ~0.0) surface water fraction. Because surface water fraction estimates are very sensitive to variations in soil moisture particularly at 6.9 GHz, in this study we do not attempt to un-mix surface water estimates below 10% (e.g. Mialon *et al* 2005).

Before determining surface water fraction, AMSR-E C-band (6.9 GHz) observations are screened for snow cover, frozen ground conditions, precipitation and radio frequency interference (RFI). The screened values are excluded from the mixture model. We use mean and standard deviation of AMSR-E brightness temperature spectral differences to identify strong RFI (Njoku *et al* 2005), while weaker signals with random occurrence may be identified by a negative MPDI. Precipitation, snow cover and frozen ground are obtained from multiband AMSR-E measurements using a decision tree approach (Zhang and Armstrong 2001, Ferraro *et al* 1996). According to the snow detection algorithm, coastal regions in Norway which are characterized by large inland water bodies and high surface topography (e.g. fjords) may not be detected as frozen ground until weeks after the initiation of snow fall. Figure 2 shows these areas with backscatter values greater than −9.5 dB for which we have not computed a surface water fraction (encircled). Moreover, very high backscatter values seen at the bottom right corner of figure 2 indicate sparsely vegetated rocky surfaces lacking open water surfaces typical for alpine mountains (e.g. Verkhoyansk range).

The remotely sensed surface fraction estimates are compared with river gauge data obtained from the Regional Integrated Hydrological Monitoring System (ArcticRIMS
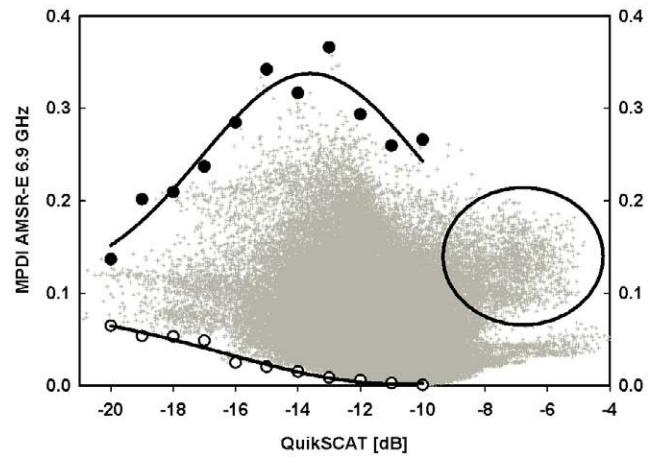

Figure 2. Relationship between AMSR-E C-band passive microwave polarization difference index (vertical axes, largely dependant on surface water fraction) and HH-polarized Ku-band QSCAT backscatter (dB) (horizontal axis, largely dependent on vegetation density) for all snow free land pixels between January 2006 and December 2007 within the study area defined as 0°–180° East and 55°–90° North. For each 1 dB range of backscatter, min and max MPDI (open and filled circles, respectively) are drawn. Sub-pixel surface water fraction is calculated based on a fully water-covered lake pixel with an MPDI of ~0.67. The contribution from the vegetation on MPDI (lower curve) varies nearly linearly between zero (at −20 dB) and 10% (at −10 dB). The large circle on the right-hand side of the graph delineates pixels which are dominated by large inland water contribution combined with high surface topography (e.g. fjords). Pixels that include snow covered areas, frozen ground conditions, precipitation, ocean areas, large lakes, coastal zones and radio frequency interference contamination have been excluded (screened) from these data.

available at http://rims.unh.edu) as well as runoff simulations using the PWBM model (Rawlins *et al* 2003). Details of these simulations, including the influence of unusually high snow water equivalent on the record discharge for the combined flow of the six largest Eurasian Rivers (Shiklomanov and Lammers 2009) are given in Rawlins *et al* (2009).

Our surface water map is compared with an 30 m resolution inundation map derived from high-resolution ALOS PALSAR imagery acquired on 11 July, 2006 along a transect in a sub-region of the Ob basin (figure 1). The PALSAR-based inundation map was aggregated to a 25 km EASE-Grid projection to facilitate comparison with the coarse-resolution surface water fraction products derived in this study. Landsat imagery and a digital elevation model (DEM) were used in conjunction with the ALOS PALSAR data to improve differentiation of open water from bare and sparsely vegetated surfaces. The synergistic use of optical and radar data is thus advantageous for accurately characterizing open water. The classification algorithm applied to the ALOS PALSAR/Landsat/DEM data was a supervised decision tree based approach adapted from the Random Forest algorithm (Breiman 2001). As verified with training data acquired for a nearby site, this classification algorithm identifies two inundated land cover classes: open water and inundated vegetation. Additional information on the classification approach is provided in Whitcomb *et al* (2009).
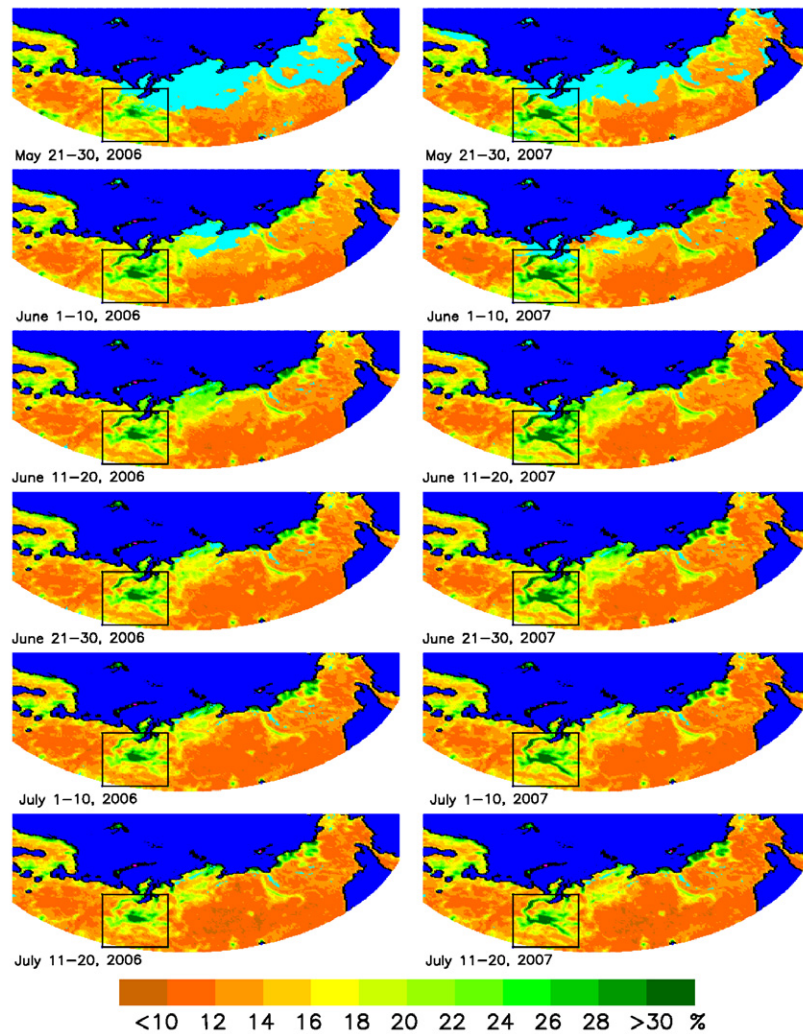
Figure 3. Evolution of mean surface water extent (%) in 2006 (left) and 2007 (right) from 21 May (top) to 20 July (bottom). Ocean (dark blue), large lakes (dark blue), coastal zones (black), RFI (light blue), bare soil (light blue) and snow (light blue) have been filtered out of these calculations.

4. Results

Surface water fraction is computed on a 10 day basis over the period January 2006 to December 2007. Figure 3 shows the surface water fractions of EASE-Grid cells from 21 May through 20 July for those years, including the springtime and early summer drainage of surface water across the study domain. Water surfaces with values above approximately 20% total surface water fraction in figure 3 notably correspond to large streams, lakes, reservoirs and poorly drained surfaces within the central Western Siberian Plain (rectangle) including ponds, swamps, bogs, mires and peats, as well as episodically inundated surfaces. Smaller concentrations of surface water are apparent along the arctic coast of Siberia and further inland. In general, surface water values in the central part of the Western Siberian Plain are higher in 2007 than in 2006, particular along River Ob.

According to a study conducted by Grippa *et al* (2007) across the same region during the summer between 1988 and 2002, there is a high positive correlation between spatially averaged surface water variations over the Ob basin and

discharge rates measured at Salekhard at the mouth of River Ob (the *R*-value was equal to 0.87). Results from 2006 and 2007 presented in figure 4 however reveal a different picture. While there appears to be a general correlation between surface water fraction over the Ob basin and river discharge after the peak in 2006, in 2007 discharge remained high after peak flow, while surface water estimates fell in the same manner as they did in 2006. This suggests that factors other than surface water extents must play a considerable role in explaining river discharge at the mouth of the basin. Indeed, strong positive net precipitation anomalies around the time of peak discharge in 2007 (Rawlins *et al* 2009) would tend to explain the higher open water fractions and discharge rates (figure 4).

Figure 5 shows simulated total runoff for April–June from the PWBM across northern Eurasia in 2006 (a) and 2007 (b). Excess runoff in 2007 has been attributed to high winter precipitation amounts and resultant snow storage, linked in turn to anomalous atmospheric circulation and moisture fluxes during winter 2006/2007 (Rawlins *et al* 2009). From these map panels it is clear that considerably more water was available for wetland recharge in 2007 than in 2006 and, moreover,
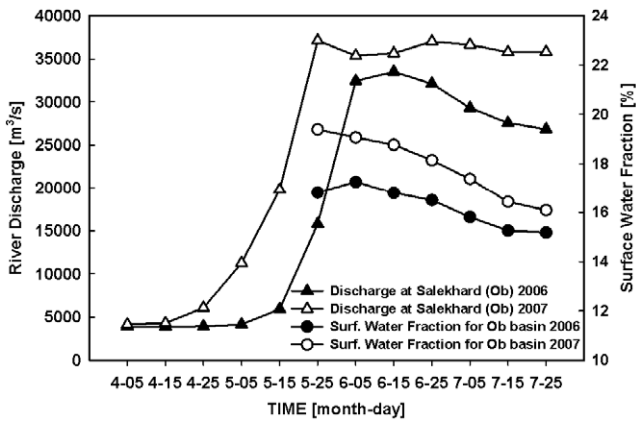
Figure 4. River discharge ($m^3\ s^{-1}$) measured at the mouth of River Ob at Salekhard before, during and after snowmelt in 2006 and 2007 compared with spatially averaged surface water fraction (%) derived from the Ob basin within the limits of our study area. Water fractions are not computed when snow coverage exceeds 5% of the total basin area.
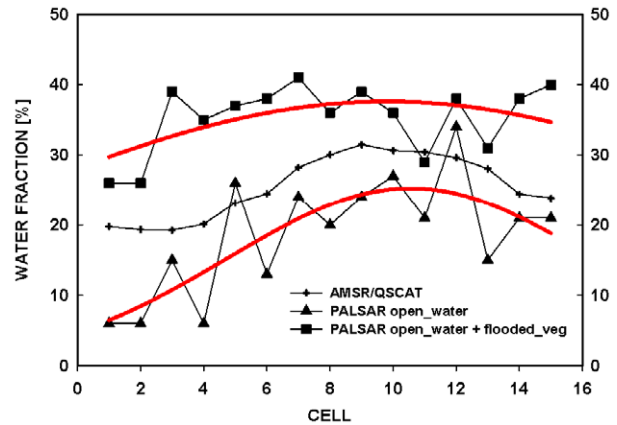

Figure 6. Direct comparison of aggregated high-resolution ALOS PALSAR surface water fraction with AMSR-E/QSCAT for a transect in a sub-region of the Ob basin. The AMSR-E/QSCAT product is sensitive to the changes in both open water and inundated vegetation. See text for a complete description.

that the wetland complexes of the central Western Siberian Plain (figure 3) are located in the region where runoff values were relatively high. The excess open water areas in 2007 would suggest significant atmospheric recycling between water bodies and the overlying atmosphere via evaporation (Serreze and Hurst 2000) and, in turn, the higher precipitation minus evaporation totals observed in May and June of 2007 (Rawlins *et al* 2009).

In figure 6, estimates of surface water fraction from AMSR-E/QSCAT are compared with surface water fraction derived from ALOS PALSAR imagery to validate the AMSR-

E/QSCAT product. The area compared is largely occupied by lakes, forest-tundra and woody floodplains in the lower Ob basin. Each AMSR-E/QSCAT point in the figure is the 25 km × 25 km EASE-Grid cell encompassing the aggregated inundation product derived from ALOS PALSAR. Figure 1 shows the location and extent of this 2-cell wide and 8-cell long transect covered by ALOS PALSAR. Cell 1 is located in the upper right corner while Cell 15 is found in the lower left corner of this transect. Cell 8 has not been used as its coverage is only partial. The ALOS PALSAR surface water fractions plotted in figure 6 were computed from inundation
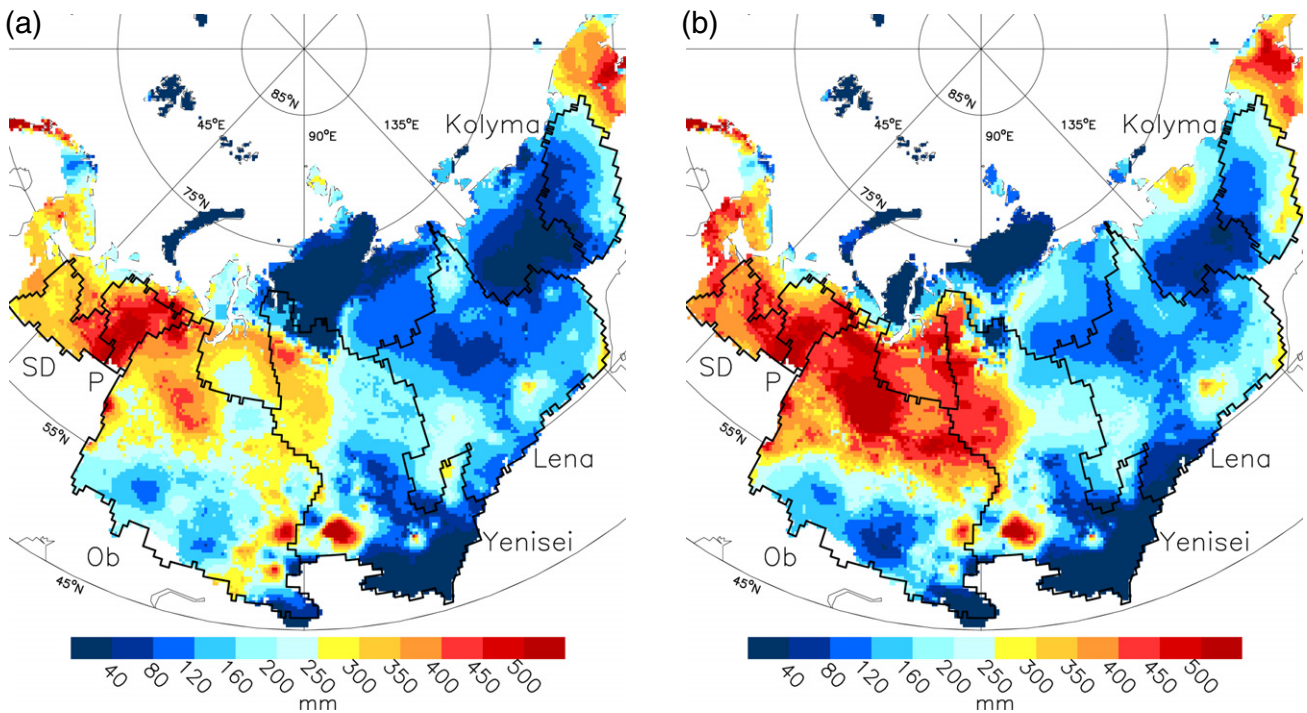

Figure 5. Total simulated runoff (mm) by the Pan-Arctic Water Balance Model for April through June 2006 (a) and 2007 (b).

mappings derived from the ALOS PALSAR imagery using the approach described in the methods description. The AMSR-E/QSCAT surface water fraction values are compared to ALOS PALSAR values derived for (1) open water only (triangles), and (2) open water plus inundated vegetation (squares), as determined from the ALOS PALSAR-based surface water classification. The difference between (1) and (2) therefore is that fraction of the landscape consisting of inundated vegetation, as observed by ALOS PALSAR. Our AMSR-E/QSCAT surface water mapping approach largely agrees with the high-resolution inundation product derived from ALOS PALSAR. The comparison shows that the AMSR-E/QSCAT product delineates not only the fraction of open water but is also sensitive to some extent to the inundated vegetation. The AMSR-E/QSCAT method shows between 2 and 8% increase in surface water fraction over the mean open water estimate made by ALOS PALSAR (bottom red curve). The AMSR-E/QSCAT approach is not able to penetrate dense vegetation as compared to the longer wavelength (L-band; 1.27 GHz frequency) ALOS PALSAR sensor, nor is it able to delineate smaller areas of surface water as is the higher-resolution PALSAR data, and as a result underestimates total surface water fraction (open water plus inundated vegetation) relative to that found by ALOS PALSAR (top red curve). The coarse AMSR-E footprint size (75 km × 43 km at 6.9 GHz) relative to the 25 km × 25 km EASE-Grid cell size to which these data sets have been posted leads to a spatial smoothing in the AMSR-E/QSCAT product that is evident when compared to the higher-resolution PALSAR product. This initial comparison is limited by currently-available PALSAR data sets as of this analysis. Assembly and classification of additional PALSAR data sets across larger areas of the study domain are on-going and will be addressed in follow-on analyses.

5. Summary and conclusion

The objective of this study was to demonstrate a capability for robust monitoring of surface water dynamics over large areas, such as demonstrated here over Northern Eurasia. Sub-pixel surface water fraction was calculated directly from C-band AMSR-E passive microwave brightness temperature data using the microwave polarization difference index (MPDI). Polarization ratios such as the MPDI are effective in separating the effects of temperature, open water and vegetation. The vegetation effect on total pixel emissivity was taken into account by incorporating HH-polarized QSCAT backscatter data. A linear mixture model was developed that allowed the computation of sub-pixel surface water fraction, utilizing several lake pixels fully covered by water.

We observe reasonable agreement between simulated land surface runoff, surface water fraction, and river discharge following snowmelt in 2006 and 2007. In 2007, large areas of the central Western Siberian Plain were extensively flooded, compared to 2006. Reported positive net precipitation anomalies during winter 2006/2007, linked in turn to excessive snow storage in 2007, are likely related to these variations. While we can only speculate, excess open water may have aided local water recycling during early summer months.

This may have helped keep river discharge rates high and contributed to greater water amounts within the wetland complexes during that time.

When compared to a high-resolution inundation map derived from ALOS PALSAR data, we found our new mapping approach shows great potential for accurate surface water mapping across Northern Eurasia. The AMSR-E/QSCAT approach was able to delineate not only variation in open water area, but also demonstrated sensitivity to variations in inundated vegetation although the sensitivity to total inundation from the longer wavelength ALOS PALSAR is not achieved. The larger nominal footprint of AMSR-E/QSCAT also tends to suppress sensitivity to spatial variability along the transect compared.

References

Breiman L 2001 Random forests *Mach. Learn.* **45** 5–32
Choudhury B J 1991 Passive microwave remote sensing contribution to hydrological variables *Surv. Geophys.* **12** 63–84
Comiso J C, Parkinson C L, Gersten R and Stock L 2008 Accelerated decline in the Arctic sea ice cover *Geophys. Res. Lett.* **35** 1–6
Ferraro R R, Weng F, Grody N C and Basist A 1996 An eight-year (1987–1994) time series of rainfall, clouds, water vapor, snow cover and sea ice derived from SSM/I measurements *Bull. Am. Meteorol. Soc.* **77** 891–905
Fily M, Royer A, Goita K and Prigent C 2003 A simple retrieval method for land surface temperature and fraction of water surface determination from satellite microwave brightness temperatures in sub-arctic areas *Remote Sens. Environ.* **85** 328–38
Frey K E and Smith L C 2003 Recent temperature and precipitation increases in West Siberia and their association with the Arctic Oscillation *Polar Res.* **22** 287–300
Giddings L and Choudhury B J 1989 Observation of hydrologic features with Nimbus-7 37 GHz data, applied to South America *Int. J. Remote Sens.* **10** 1673–86
Grippa M, Mognard N M, Le Toan T and Biancamaria S 2007 Observations of changes in surface water over the western Siberia lowland *Geophys. Res. Lett.* **34** 1–5
Jones L A, Kimball J S, McDonald K C, Chan S T K, Njoku E G and Oechel W C 2007 Satellite microwave remote sensing of boreal and arctic soil temperatures from AMSR-E *IEEE Trans. Geosci. Remote Sens.* **45** 2004–18
Kimball J S, McDonald K C, Running S W and Frolking S 2004 Satellite radar remote sensing of seasonal growing seasons for boreal and sub-alpine evergreen forests *Remote Sens. Environ.* **90** 243–58
Kimball J S, McDonald K C and Zhao M 2006 Spring thaw and its effect on northern terrestrial vegetation productivity observed from satellite microwave and optical remote sensing *Earth Interact.* **10** 1–22

Knowles K W, Savoie M H, Armstrong R L and Brodzik M J 2006 *Updated to 2009 AMSR-E/Aqua Daily EASE-Grid Brightness Temperatures (Boulder, CO, January 2006–December 2007)* National Snow and Ice Data Center (Digital media)

Mialon A, Royer A and Fily M 2005 Wetland seasonal dynamics and interannual variability over northern high latitudes, derived from microwave satellite data *J. Geophys. Res.* **110** 1–9

Njoku E G, Ashcroft P, Chan T K and Li Li 2005 Global survey and statistics of radio-frequency interference in AMSR-E land observations *IEEE Trans. Geosci. Remote Sens.* **43** 938–47

Njoku E G, Jackson T J, Lakshmi V, Chan T K and Nghiem S V 2003 Soil moisture retrieval from AMSR-E *IEEE Trans. Geosci. Remote Sens.* **41** 215–29

Pavelsky T M and Smith L C 2008 Remote sensing of hydrologic recharge in the Peace-Athabasca delta, Canada *Geophys. Res. Lett.* **35** 1–5

Peterson B J, Holmes R M, McClelland J W, Vörösmarty C J, Lammers R B, Shiklomanov A I, Shiklomanov I A and Rahmstorf S 2002 Increasing river discharge to the Arctic Ocean *Science* **298** 2171–3

Prigent C, Matthews E, Aires F and Rossow W B 2001 Remote sensing of global wetland dynamics with multiple satellite data sets *Geophys. Res. Lett.* **28** 4631–4

Rawlins M A, Lammers R B, Frolking S, Fekete B M and Voeroesmarty C J 2003 Simulating pan-Arctic runoff with a macro-scale terrestrial water balance model *Hydrol. Process.* **17** 2521–39

Rawlins M A, Serreze M C, Schroeder R, Zhang X and McDonald K C 2009 Diagnosis of the record discharge of Arctic-draining Eurasian Rivers in 2007 *Environ. Res. Lett.* **4** 045011

Richter-Menge J *et al* 2008 *Arctic Report Card 2008* www.arctic.noaa.gov/reportcard

Romanovsky V E, Burgess M, Smith S, Yoshikawa K and Brown J 2002 Permafrost temperature records: indicator of climate change *Eos, Trans. AGU* **83** 589

Serreze M C and Hurst C M 2000 Representation of mean Arctic precipitation from NCEP-NCAR and ERA reanalysis *J. Clim.* **13** 182–201

Serreze M C, Maslanik J A, Scambos T A, Fetterer F, Stroeve J, Knowles K, Fowler C, Drobot S, Barry R G and Haran T M 2003 A record minimum arctic sea ice extent and area in 2002 *Geophys. Res. Lett.* **30** 1110

Serreze M C, Walsh J E, Chapin F S III, Osterkamp T, Dyurgerov M, Romanovsky V, Oechel W C, Morison J, Zhang T and Barry R G 2000 Observational evidence of recent change in the northern high latitude environment *Clim. Change* **46** 159–207

Shiklomanov A I and Lammers R B 2009 Record Russian river discharge in 2007 and the limits to analysis *Environ. Res. Lett.* **4** 045015

Sippel S J, Hamilton S K, Melack J M and Choudhury B J 1994 Determination of inundation area in the Amazon river floodplain using the SMMR 37 GHz polarization difference *Remote Sens. Environ.* **48** 70–6

Smith L C, Sheng Y, MacDonald G M and Hinzman L D 2005 Disappearing Arctic Lakes *Science* **308** 1429

Temimi M, Leconte R, Brissette F and Chaouch N 2005 Flood monitoring over the Mackenzie River Basin using passive microwave data *Remote Sens. Environ.* **98** 344–55

Walter K M, Zimov S A, Chanton J P, Verbyla D and Chapin F S III 2006 Methane bubbling from Siberian thaw lakes as a positive feedback to climate warming *Nature* **443** 71–5

Whitcomb J, Moghaddam M, McDonald K C, Kellndorfer J and Podest E 2009 Mapping vegetated wetlands of Alaska using L-band radar satellite imagery *Can. J. Remote Sens.* **35** 54–72

Zhang K, Kimball J S, McDonald K C, Cassano J J and Running S W 2007 Impacts of large-scale oscillations on pan-Arctic terrestrial net primary production *Geophys. Res. Lett.* **34** L21403

Zhang T and Armstrong R L 2001 Soil freeze/thaw cycles over snow-free land detected by passive microwave remote sensing *Geophys. Res. Lett.* **28** 763–6

Zhang X, Sorteberg A, Zhang J, Gerdes R and Comiso J C 2008 Recent radical shifts of atmospheric circulations and rapid changes in Arctic climate system *Geophys. Res. Lett.* **35** L22701

Zimov S A, Schuur E A and Chapin F S 2006 Climate change: permafrost and the global carbon budget *Science* **312** 1612–13

Zimov S A, Voropaev Y V, Semiletov I P, Davidov S P, Prosiannikov S F, Chapin F S III, Chapin M C, Trumbore S and Tyler S 1997 North Siberian Lakes: a methane source fueled by Pleistocene carbon *Science* **277** 800–2